CrossMark

Electrocatalytic activities of alkyne-functionalized copper nanoparticles in oxygen reduction in alkaline media

Ke Liu, Yang Song, Shaowei Chen*

Department of Chemistry and Biochemistry, University of California, 1156 High Street, Santa Cruz, CA 95064, USA

HIGHLIGHTS

- Copper nanoparticles stabilized by self-assembly of alkynes onto the Cu surface.
- Formation of Cu−C≡ interfacial bonds as manifested by FTIR and PL measurements.
- Formation of metal oxides within the Cu nanoparticles revealed in XPS studies.
- Electrocatalytic activity in oxygen reduction by the Cu nanoparticles in 0.1 M NaOH.
- Best performance observed with nanoparticles with the least amount of metal oxides.

ARTICLE INFO

ABSTRACT

Stable alkyne-capped copper nanoparticles were prepared by chemical reduction of copper acetate with sodium borohydride in the presence of alkyne ligands. Transmission electron microscopic measurements showed that nanoparticles were well dispersed with a diameter in the range of 4–6 nm. FTIR and photoluminescence spectroscopic measurements confirmed the successful attachment of the alkyne ligands onto the nanoparticle surface most likely forming Cu−C≡ interfacial bonds. XPS measurements indicated the formation of a small amount of CuO in the nanoparticles with a satellite peak where the binding energy red-shifted with increasing Cu(II) concentration. Cu_2O was also detected in the nanoparticles. Similar results were observed with commercial CuO nanoparticles. Electrochemical studies showed that the as-prepared alkyne-capped copper nanoparticles exhibited apparent electrocatalytic activity in oxygen reduction in alkaline media, a performance that was markedly better than those reported earlier with poly- or single-crystalline copper electrodes; and the fraction of peroxides in the final products decreased with decreasing concentration of oxide components in the nanoparticles.

© 2014 Elsevier B.V. All rights reserved.

1. Introduction

Proton exchange membrane fuel cells are clean and environmental-friendly power sources [1,2]. For hydrogen fuel cells, with a large Gibbs free energy of −273.13 kJ mol^{-1}, the reaction of hydrogen and oxygen is thermodynamically favorable and expected to exhibit a high theoretical efficiency on energy conversion. However, as oxygen reduction reactions (ORR) on the cathode are kinetically sluggish, the reactions can proceed only at significantly large overpotentials and consequently compromise the overall efficiency [3]. Platinum-based nanoparticles have been used extensively as the catalysts of choice for ORR [4–7]; and a variety of strategies have been reported in the literature to further improve the ORR activities, such as rational design and preparation of Pt-based alloys [8] and surface engineering of Pt nanoparticles by selected organic ligands [9–11]. This is motivated by a deliberate balance between surface accessibility of active sites and control of electronic structures of the metal cores which may manipulate the adsorption and reduction of oxygen. Meanwhile, owing to the high price and scarcity of platinum, extensive efforts have also been focused on Pt-free catalysts such as transition metal oxides and chalcogenides [12,13], pyrolyzed metal macrocycles [14,15], N-doped carbon nanostructures [16], etc. Among these, studies of copper-based electrocatalysts for ORR have been relatively scarce. In fact, copper has been largely used as a supporting substrate or non-active component in the electrocatalytic reduction of oxygen [17–21]. Yet, using a polycrystalline copper electrode, Schiffrin and coworkers [22,23] have shown that the electrode exhibited apparent electrocatalytic activity in oxygen reduction in a borax buffer solution, though at a large overpotential, and proposed that

surface redox couples like Cu_2O/CuO played an important role in the reduction sequence with a CE mechanism whereas direct electron transfer to oxygen might occur from the oxide-free electrode surface. Brisard et al. [24,25] also observed electrocatalytic activity of Cu(100) and Cu(111) single-crystal electrodes in oxygen reduction in sulfuric acid where the reaction kinetics was impacted by the adsorption of (bi)sulfate ions on the electrode surface. In a more recent study [26], it was reported that cuprous oxide nanoparticles might serve as efficient catalyst for oxygen reduction; however, no detailed mechanism was included. Nevertheless, these earlier studies suggest that partial oxidation of copper surfaces might be a key step in enhancing the adsorption and eventual electroreduction of oxygen on copper. This is the primary motivation of the present study.

Herein we prepared alkyne-capped copper nanoparticles by reducing copper acetate with sodium borohydride in the presence of alkyne ligands at two temperatures, 0 °C and room temperature. 1-Decyne was chosen as the illustrating example, primarily because (i) the acetylene moiety can self-assemble onto copper surfaces forming relatively strong metal-ligand interfacial bonds, and (ii) the chainlength of the ligands is long enough to stabilize the nanoparticles and yet not too long to inhibit electron transfer in ORR studies. Transmission electron microscopic (TEM) studies showed that as-prepared copper nanoparticles were well separated, suggesting effective protection of the nanoparticles by the alkyne ligands; and the nanoparticle diameters were found to be in the range of 4–6 nm. FTIR and photoluminescence spectroscopic measurements confirmed the bonding attachment of the alkyne ligands onto the nanoparticle surface most likely forming Cu−C≡ interfacial bonds. XPS measurements revealed the formation of a small amount of CuO in the nanoparticles with the concentration higher in the samples prepared at ambient temperature than that at 0 °C. Cu_2O was also identified in the nanoparticles, as well as in commercial CuO nanoparticles. Electrochemical studies indicated that the 0 °C samples exhibited the best electrocatalytic activity in oxygen reduction among the three in 0.1 M NaOH. This was accounted for by the low oxide concentration within the nanoparticles and the ready formation of Cu_2O that likely facilitated the further reduction of peroxide into hydroxide.

2. Experimental section

2.1. Chemicals

Copper acetate $(Cu(OAc)_2 \cdot H_2O$, 99.9%, Alfa Aesar), 1-decyne (HC10, TCI America), sodium borohydride ($NaBH_4$, ≥98%, ACROS), and copper oxide nanopowders (CuO, 99%, dia. ~40 nm, SkySpring Nanomaterials) were all used as received without any further purification. Solvents were purchased at the highest purity available from typical commercial sources and also used as received. Water was deionized with a Barnstead Nanopure water system (18.3 MΩ cm).

2.2. Synthesis of copper nanoparticles

In a typical synthesis, 0.1 mmol of copper acetate was dissolved in 2 mL of water, into which was added a 10-fold molar excess of 1-decyne dissolved in 10 mL of ethanol and 50 mL of dichloromethane. This solution was kept either in an ice-water bath or at ambient temperature, into which was added dropwise 1 mmol of $NaBH_4$ (37.8 mg) dissolved in 2 mL of water under vigorous stirring and N_2 protection. In both syntheses, the originally blue solutions were found to turn green, light yellow, brown and finally black during the course of $NaBH_4$ addition. After three hours of magnetic stirring, the solutions were dried under rotary evaporation and the

solids were washed with methanol five times to remove excessive ligands and reaction byproducts, affording purified 1-decyne-protected copper nanoparticles that were denoted as CuHC10-IB and CuHC10-RT, respectively. The nanoparticles were found to be readily dispersible in apolar solvents such as CH_2Cl_2, $CHCl_3$, THF, toluene, etc, but insoluble in polar solvents like alcohols, acetone, and acetonitrile.

2.3. Characterizations

The morphology and sizes of the nanoparticles were characterized by transmission electron microscopic studies (TEM, Philips CM300 at 300 kV). UV−vis spectroscopic studies were performed with an ATI Unicam UV4 spectrometer using a 1 cm quartz cuvette at a resolution of 2 nm. Photoluminescence characteristics were examined with a PTI fluorospectrometer. FTIR measurements were carried out with a Perkin−Elmer FTIR spectrometer (Spectrum One, spectral resolution 4 cm^{-1}), where the samples were prepared by casting the particle solutions onto a ZnSe disk. The crystalline properties of the nanoparticle catalysts were evaluated by powder X-ray diffraction (XRD) measurements with a Rigaku Mini-flex Powder Diffractometer using Cu-Kα radiation with a Ni filter ($\lambda = 0.154059$ nm at 30 kV and 15 mA). X-ray photoelectron spectra (XPS) were recorded with a PHI 5400/XPS instrument equipped with an Al Kα source operated at 350 W and 10^{-9} Torr. Silicon wafers were sputtered by argon ions to remove carbon from the background and used as substrates.

2.4. Electrochemistry

Electrochemical tests were carried out in a standard three-electrode cell connected to a CHI 710C electrochemical work station, with a Pt foil counter electrode and a saturated calomel electrode (SCE) reference electrode. The working electrode is a rotating platinum ring-glassy carbon disk electrode (RRDE, disk diameter 5.61 mm, from Pine Instrument). To prepare catalyst solutions for oxygen reduction tests, dilute solutions of Cu nanoparticles in toluene were mixed with XC-72 carbon black and a Nafion 117 solution (5 wt.%, Fluka) to form a well-dispersed catalyst "ink" (Pt:carbon black = 1:4 (w/w), Nafion: 0.05%) under ultrasound. A calculated amount of the catalyst ink was slowly dropcast onto the glassy carbon disk electrode of the RRDE, at a metal loading of 15 µg for each nanoparticle catalyst. When the electrode was dried, a dilute Nafion solution (0.1 wt.%, 3 µL) was added onto the surface. The electrode was then dried in air and immersed into electrolyte solutions for electrochemical tests.

3. Results and discussion

Fig. 1 depicts a representative TEM micrograph of the (A) CuHC10-IB and (B) CuHC10-RT nanoparticles. It can be seen that both Cu nanoparticles are roughly spherical and well separated, suggesting successful attachment of the alkyne ligands on the Cu nanoparticle surface forming stable nanoparticles. Additionally, statistical analysis based on more than 100 nanoparticles showed that the average diameter of the nanoparticles synesized at room temperature (CuHC10-RT) was 4.28 ± 0.46 nm, whereas for the nanoparticles prepared at a lower temperature (CuHC10-IB), the size was somewhat larger at 6.29 ± 0.99 nm, as manifested in the respective figure insets. Note that for organically capped metal nanoparticles, the size of the nanoparticles is largely determined by two competing processes, nucleation of metal atoms to form the nanoparticle cores and passivation of the metal cores by organic capping ligands that impedes the core growth [27]. For mercapto-stabilized gold nanoparticles, typically the lower the reaction
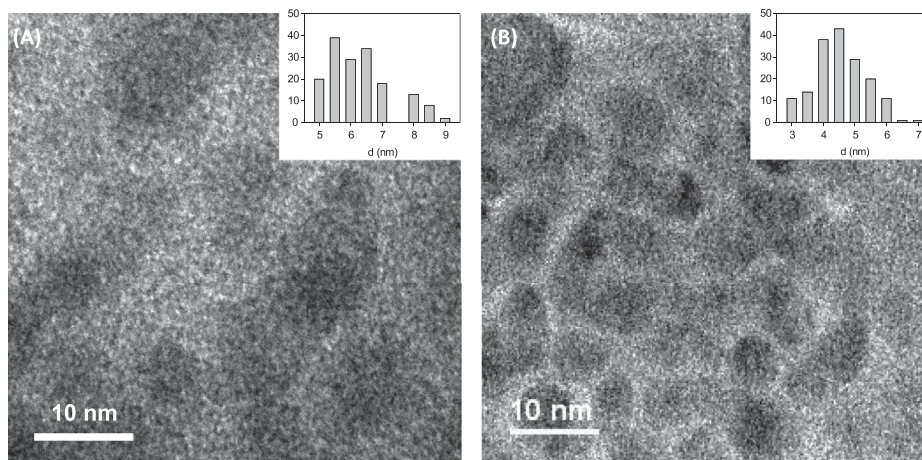
Fig. 1. Representative TEM micrographs of (A) CuHC10-IB and (B) CuHC10-RT nanoparticles. Scale bars 10 nm. Insets show the corresponding core size histograms.

temperature, the smaller the nanoparticle cores [28]. This is ascribed to the strong affinity of thiol moieties to gold surfaces and thus the reductive formation and nucleation of gold atoms plays a significant role in the determination of the eventual size of the nanoparticles. The behaviors are completely different with the decyne-stabilized copper nanoparticles in the present study. In the formation of CuHC10 nanoparticles, the adsorption of alkyne ligands onto the copper surface was relatively slow; thus the passivation of the growth of the copper nanoparticles was most likely to be enhanced at higher temperatures, leading to a smaller size of the nanoparticles, as observed above.

The successful passivation of the copper nanoparticles by the decyne ligands is further manifested in FTIR measurements, as shown in Fig. 2. Note that the FTIR spectra were almost identical for both CuHC10-RT and CuHC10-IB nanoparticles, so only the one of CuHC10-RT was shown here (black curve), along with that of the 1-decyne monomers (red curve). From the figure it can be see that the $\equiv$C–H vibrational stretch at 3312 cm^{-1} was well-defined for the monomeric ligands of 1-decyne; yet this feature vanished with the nanoparticle samples suggesting efficient breaking of the $\equiv$C–H bond after the alkyne ligands were adsorbed onto the copper

nanoparticle surface (the absence of this vibrational feature in the spectrum also indicates that the nanoparticles were free of excessive alkyne ligands). Additionally, for monomeric 1-decyne ligands, the C$\equiv$C vibrational stretch can be identified at 2120 cm^{-1}; yet for the CuHC10 nanoparticles, this band appears to red-shift to 1720 cm^{-1}, most likely as a result of the cleavage of the $\equiv$C–H bond and the formation of Cu–C$\equiv$ interfacial linkages, where the conjugated metal-ligand bonds led to effective intraparticle charge delocalization between the particle-bound acetylene moieties and hence a decreasing bonding order of the C$\equiv$C moieties, as observed in previous studies [11,29,30]. Furthermore, with this interfacial configuration, the small shoulder at 1930 cm^{-1} may be assigned to Cu–H bonds, which is consistent with the Cu–H vibrational stretch that has been identified at 1940 cm^{-1} in a previous study of crystalline metal hydrides [31]. Another discrepancy is the antisymmetric (d$_-$) and symmetric (d$_+$) CH$_2$ vibrational stretches which can be found at 2927 and 2856 cm^{-1}, respectively, for the monomeric ligands, but red-shifted somewhat to 2920 and 2850 cm^{-1}, as a result of increasing packing order of the molecules adsorbed on the nanoparticle surface.

The formation of conjugated metal-ligand interfacial linkages is also evidenced in photoluminescence measurements. Fig. 3 depicts the excitation and emission spectra of the CuHC10-RT (black curves) and CuHC10-IB (red curves) nanoparticles in CHCl$_3$. It can be seen that both nanoparticles exhibited a pair of rather well-defined excitation and emission peaks at almost identical positions of λ_{ex} = 416 nm and λ_{em} = 480 nm, respectively. Similar photoluminescence behaviors have also been observed with alkyne-functionalized Pt and Ru nanoparticles and ascribed to the formation of conjugated metal-ligand bonds that led to extensive intraparticle charge delocalization. Therefore, the particle-bound acetylene moieties behaved analogously to diacetylene (C$\equiv$C–C$\equiv$C) derivatives [11,32]. Yet one may notice that for decyne-functionalized Ru nanoparticles, the excitation and emission peak positions are typically found at 360 and 440 nm [32], and for the corresponding Pt nanoparticles, at 352 nm and 430 nm [11]. This discrepancy may be correlated with the electrical resistivity of the metals (at 0 °C) [33] that increases in the order of 1.543×10^{-8} Ωm for Cu < 7.1×10^{-8} Ωm for Ru < 9.6×10^{-8} Ωm for Pt, where the intraparticle charge delocalization is facilitated by the conducting metal cores, and a decreasing resistivity leads to a red-shift of the excitation and emission peak energies.

The chemical nature of the resulting nanoparticles was then examined by XPS measurements. Fig. 4(A) shows the full survey spectra of the CuHC10-IB, CuHC10-RT, and commercial CuO
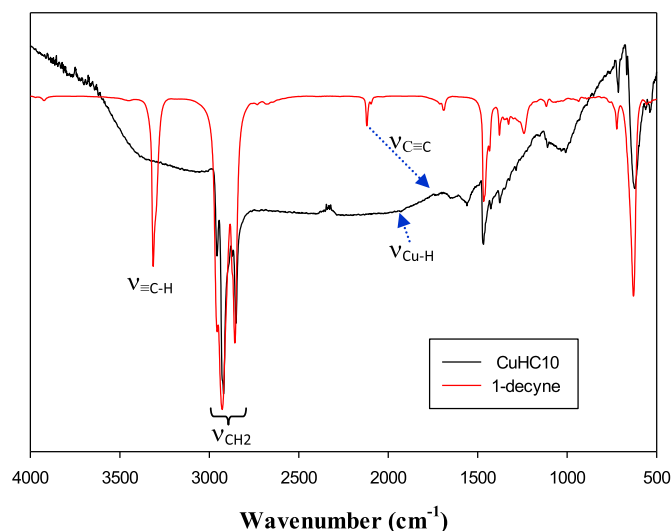

Fig. 2. FTIR spectra of CuHC10 nanoparticles (black curve) and monomeric 1-decyne ligands (red curve). (For interpretation of the references to color in this figure legend, the reader is referred to the web version of this article.)
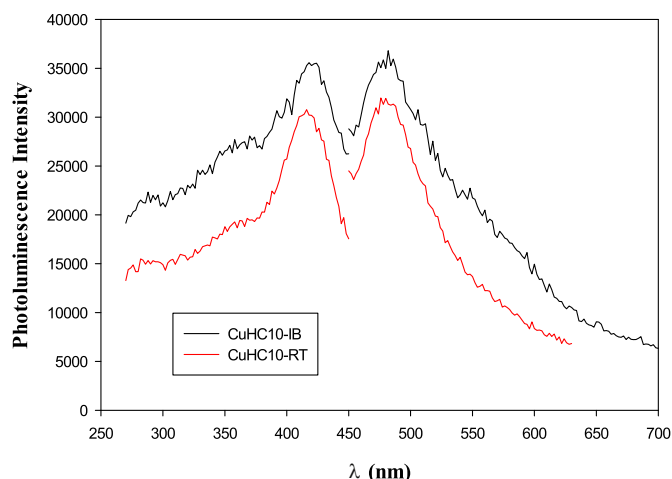
Fig. 3. Excitation and emission spectra of CuHC10-RT and CuHC10-IB nanoparticles in CHCl₃. (For interpretation of the references to color in this figure legend, the reader is referred to the web version of this article.)

Fig. 4. (A) XPS survey spectra and (B) high-resolution scans of the Cu2p electrons of CuHC10-IB, CuHC10-RT and commercial CuO nanoparticles. In panel (B), black curves are the raw experimental data and color curves are the deconvolution fits. (For interpretation of the references to color in this figure legend, the reader is referred to the web version of this article.)

Table 1
Binding energies (eV) of the Cu2p electrons and the ratio ($x_{Cu(II)}$) of Cu(II) over Cu(I) and Cu(0) combined in CuHC10-IB, CuHC10-RT and commercial CuO nanoparticles.

	Cu2p3/2	Cu2p1/2	Satellite	$x_{Cu(II)}$
CuHC10-IB	932.93	952.78	946.91	7.1%
CuHC10-RT	933.47	953.61	943.50	26.2%
Commercial CuO	932.99	953.13	941.13	50.1%

nanoparticles. For all samples, the Cu2p electrons can be identified at the twin peaks of 933 eV and 953 eV and the C1s electrons at about 284 eV. Interestingly, both decyne-capped copper nanoparticles exhibit a broad peak centered at around 570 eV, suggesting possible formation of cuprous oxide within the nanoparticles as the Cu LMM-2 auger transitions are typically found around 568 and 570 eV for metallic Cu and Cu₂O, respectively [34]. In fact, the O1s electrons can be readily found at around 530 eV.

High-resolution scans of the Cu2p electrons are depicted in panel (B), from which two main peaks may be identified at around 933 and 953 eV for all samples, as summarized in Table 1. These may be assigned to the Cu2p3/2 and Cu2p1/2 electrons, respectively, which are consistent with those of metallic copper and cuprous oxide, as the binding energies of the Cu2p electrons for Cu(0) and Cu(I) are only 0.1 eV apart [35]. In fact, XRD measurements clearly showed the presence of both Cu and Cu₂O in the nanoparticle samples (Figure S1, Supplementary Information). This is also consistent with the appearance of the LMM-2 auger transitions at around 570 eV as observed above in panel (A). In addition, all samples exhibited a satellite peak between the two main peaks, yet at different positions: 946.91 eV for the CuHC10-IB nanoparticles, 943.50 eV for CuHC10-RT, and 941.59 eV for the commercial CuO nanoparticles. This is consistent with that of CuO, indicating the formation of a small fraction of cupric oxide in the nanoparticles, as the satellite peak is typically observed in ions with a partially filled 3d shell but absent in ions with a completely filled 3d shell [36]. Furthermore, the increasing intensity of the satellite peaks suggests the increasing concentration of the Cu(II) species, as depicted in Fig. 4(B). In fact, based on the integrated peak areas, the ratio of Cu(II) over Cu(I) and Cu(0) combined in the nanoparticles is estimated to be 7.1%, 26.2%, and 50.1% in CuHC10-IB, CuHC10-RT, and commercial CuO nanoparticles, respectively (Table 1).

Note that the appearance of the satellite peak has been largely ascribed to the shake-up effect where the outgoing electron interacts with a valence electron and excites it to a higher energy level [36]. Therefore, the observed red-shift of the satellite peaks, CuHC10-IB (946.91 eV) > CuHC10-RT (943.50 eV) > commercial CuO nanoparticles (941.59 eV), is consistent with the increasing content of the Cu(II) components that exhibit a vacant 3d orbital, in contrast to Cu(I) or Cu(0) that features a 3d¹⁰ electronic configuration with 4s being the lowest-energy empty orbital.

Interestingly, the nanoparticles synthesized above were found to exhibit apparent electrocatalytic activity in the reduction of oxygen. Note that prior to electrochemical measurements, the nanoparticles-modified electrodes were subject to about 100 potential cycles within the potential range of +0.5 V to +0.1 V (vs RHE) in order to desorb part of the protecting ligands and expose the nanoparticle cores. Fig. 5 shows the steady-state cyclic voltammograms of the electrodes modified with the three nanoparticle catalysts in a N₂-saturated 0.1 M NaOH solution. From the figure, one can see that at the CuHC10-IB electrode (black curve), two anodic peaks are well-defined at around +0.55 V and +0.84 V (vs RHE). The former is believed to correspond to the formation of a monolayer of Cu₂O while the latter to the formation of a thick multilayer film of CuO, and the cathodic peak at around +0.60 V is
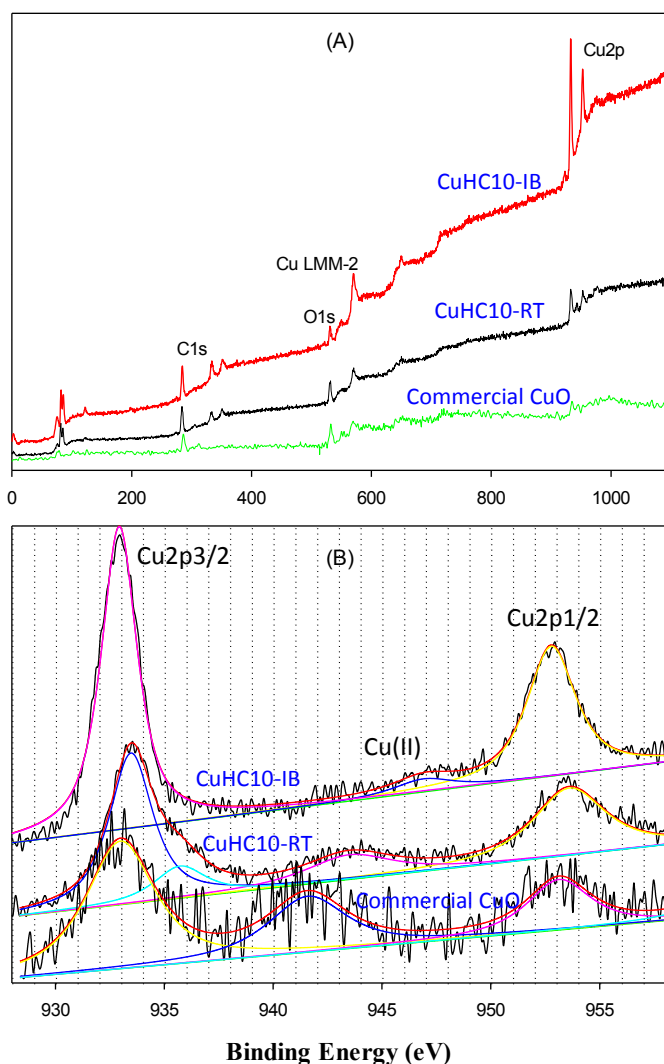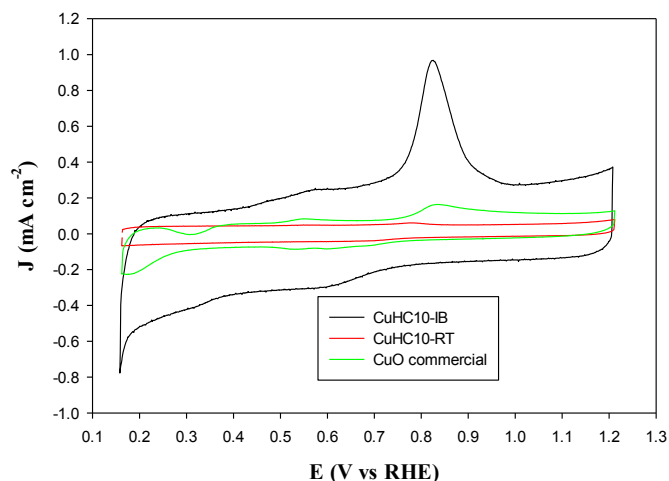
Fig. 5. Cyclic voltammograms of a glassy carbon disk electrode modified with 15 μg of CuHC10-IB (black curve), CuHC10-RT (red curve) and commercial CuO (green curve) nanoparticles in a nitrogen-saturated 0.1 M NaOH solution. Nanoparticle loading is all 15 μg and potential scan rate is 0.01 V s^{-1}. (For interpretation of the references to color in this figure legend, the reader is referred to the web version of this article.)

likely to originate from the partial reduction of CuO to Cu$_2$O [37]. Similar features can also be seen with the CuHC10-RT electrode (red curve) and the commercial CuO nanoparticles (green curve) but at much lower current amplitudes. This seems to suggest more efficient electrochemical desorption of ligands from the CuHC10-IB nanoparticle surface than from CuHC10-RT, likely a result of somewhat stronger metal-ligand ($d_\pi-p_\pi$) interactions in the latter with the higher Cu(II) content.

Fig. 6 depicts the RRDE voltammograms of a platinum ring-glassy-carbon disk electrode with the disk modified with a calculated amount of (A) CuHC10-IB, (B) CuHC10-RT, and (C) commercial CuO nanoparticles in an O$_2$-saturated 0.1 M NaOH solution at different rotation rates. It can be seen that on the disk electrode the cathodic currents start to increase at sufficiently negative potentials, indicating apparent electrocatalytic activity of the three nanoparticles in oxygen reduction. Yet it can be seen that the onset potential for oxygen reduction is different among the three nanoparticle catalysts, at +0.83 V for CuHC10-IB, +0.82 V for CuHC10-RT, and +0.81 V for commercial CuO nanoparticles, suggesting that CuHC10-IB nanoparticles was the best among the series. Note that at these potentials, (partial) reduction of CuO into Cu$_2$O occurred, indicating unlikely involvement of CuO in oxygen reduction [22,23].

Furthermore, the corresponding ring currents were all at least an order of magnitude lower. From the ratio of the ring current (I_R) and disk current (I_D), the number of electron transfer (n) during oxygen reduction can be estimated by $n = 4I_D/(I_D + I_R/N)$, and concurrently the percentage of peroxide formed in the reduction products by $x_{H_2O_2}(\%) = 200(1 - n/4)$, with N being collection efficiency (37%) [9], which are depicted in Fig. 7. It can be seen that the electrode potential at which $n = 2$ (corresponding to the 2 electron reduction of oxygen into peroxide species) is markedly different, +0.83 V for CuHC10-IB, +0.73 V for CuHC10-RT, and +0.75 V for commercial CuO nanoparticles, again signifying the best performance of the CuHC10-IB nanoparticles. At more negative potentials, the n values increases accordingly. For instance, within the potential range of +0.70 V to +0.40 V, the n values were rather consistent at 2.5–2.7 for the three nanoparticle catalysts, suggesting the formation of both peroxide and hydroxide as the final products of oxygen reduction. In fact, peroxides account for about 70% of the final products, indicating that oxygen reduction
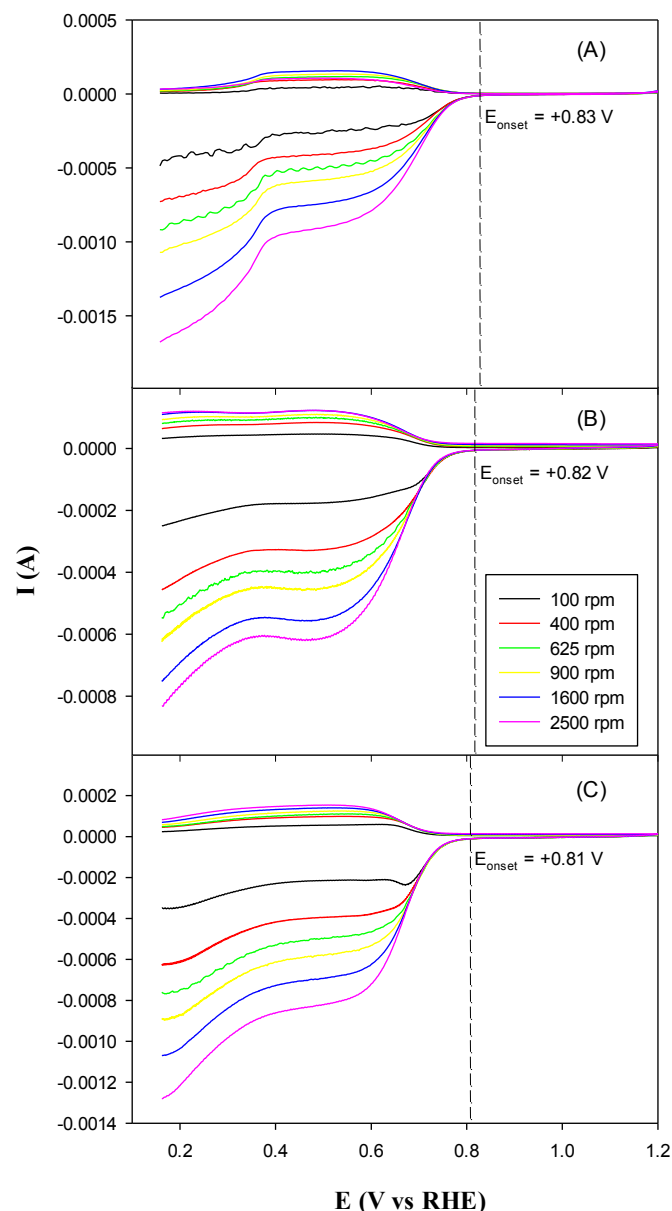

Fig. 6. RRDE voltammograms of a platinum ring-glassy-carbon disk electrode with the disk modified with (A) CuHC10-IB, (B) CuHC10-RT, and (C) commercial CuO nanoparticles in an oxygen-saturated 0.1 M NaOH solution. Nanoparticle loading is all 15 μg. Electrode rotation rates are specified in the figure legends. Ring currents are collected by setting the ring potential at +1.3 V vs RHE. Dashed lines highlight the onset potentials (E_{onset}).

proceeded with a mixture of the 2- and 4-electron reduction pathways. Note that the reduction of Cu$_2$O to Cu occurred in this same potential range (Fig. 5), and it has been proposed that Cu$_2$O might be involved in the reduction of peroxide intermediates with a CE mechanism [22,23]. At even more negative potentials (<+0.30 V) where reduction of Cu$_2$O to Cu is likely to take place, the n value reached 3.5 for CuHC10-IB nanoparticles (and $x_{H_2O_2}$ exhibited an apparent diminishment down to <20%), markedly higher than those for CuHC10-RT and CuO nanoparticles. This indicates that the formation of peroxides as the reduction products became minimal, with increasing metallic characters of the catalyst surface. This transition of the n values (and hence the products of oxygen reduction) is consistent with the two plateaus observed in RRDE voltammetric measurements in Fig. 6.
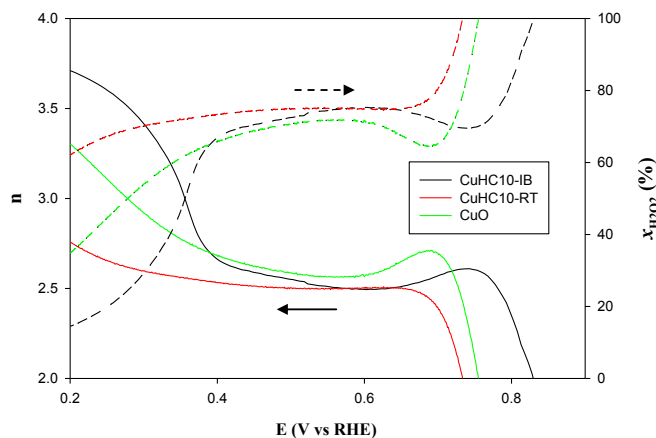
Fig. 7. Variation of the number of electron transfer (n, solid curves, left *y* axis) and percentage ($x_{H_2O_2}$, dashed curves, right *y* axis) of peroxide formed in oxygen reduction with electrode potential for CuHC10-IB (black curves), CuHC10-RT (red curves) and commercial CuO (green curves) nanoparticles. Data were calculated from the RRDE voltammograms at 1600 rpm in Fig. 6. (For interpretation of the references to color in this figure legend, the reader is referred to the web version of this article.)
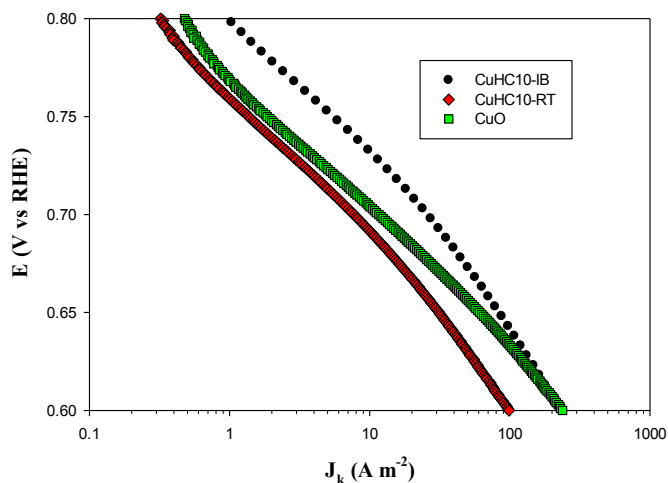

Fig. 8. Tafel plots of oxygen reduction catalyzed by CuHC10-IB (black circles), CuHC10-RT (red diamonds) and commercial CuO (green squares) nanoparticles. Data are acquired from linear regressions of the Koutecky−Levich plots based on the original data in Fig. 6. (For interpretation of the references to color in this figure legend, the reader is referred to the web version of this article.)

Further insights into the electron transfer kinetics of oxygen reduction were revealed by Koutecky−Levich analysis, as the RRDE voltammetric currents include both kinetic current (I_k) and diffusion (I_d) controlled contributions [38],

$$\frac{1}{I_D} = \frac{1}{I_k} + \frac{1}{I_d} = \frac{1}{I_k} + \frac{1}{B\omega^{1/2}} \tag{1a}$$

$$B = 0.62nFAC_O D_O^{2/3} \nu^{-1/6} \tag{1b}$$

$$I_k = nAFkC_O \tag{1c}$$

where ω is the electrode rotation rate, *n* is the overall number of electron transfer, F is Faraday constant, C_O is the bulk concentration of O_2 dissolved in the electrolyte, D_O is the diffusion coefficient of O_2, and ν is the kinetic viscosity of the electrolyte. For all three nanoparticle catalysts, plots of I^{-1} vs $\omega^{-1/2}$ show good linearity and parallelism within the potential range of +0.80 to +0.60 V (not shown), indicating first order reaction with respect to dissolved oxygen. From the intercepts of the linear regression, the corresponding kinetic current densities (J_k, I_k normalized by the electrode surface area) can also be evaluated, as depicted in the Tafel plot of Fig. 8. It can be seen that the kinetic currents within the potential range of +0.80 to +0.60 V increase in the order of commercial CuO < CuHC10-RT < CuHC10-IB, again, indicating the best electrocatalytic performance of the CuHC10-IB nanoparticles.

In addition, linear regressions of the Tafel plots yield a slope of 82.7 mV dec^{-1} for CuHC10-IB, 76.2 mV dec^{-1} for CuHC10-RT, and 69.3 mV dec^{-1} for commercial CuO nanoparticles. Note that for oxygen electroreduction at nanoparticle catalyst surfaces, the Tafel slopes are typically found at 60 mV dec^{-1} or 120 mV dec^{-1}, where the former corresponds to a pseudo two-electron reaction as the rate determining step, and in the latter the rate determining step is presumed to be the first-electron reduction of oxygen [1]. Therefore it is likely that oxygen reduction on the copper nanoparticle surface proceeded by the pseudo two-electron route. This is consistent with the above observation that peroxide derivatives constituted a rather large portion of the final products in the low overpotential regime (Fig. 7). It is known that adsorption of O_2 on completely oxidized surfaces is energetically unfavorable and thus a high

overpotential is required for oxygen reduction to proceed. Within this context, the higher the CuO component in the copper nanoparticles, the lower the catalytic activity in oxygen reduction. In addition, it has been suggested that Cu_2O may donate electrons to oxygen and serve as effective catalysts for ORR [26]; and from Fig. 5, one can see the voltammetric peak currents for the formation of Cu_2O (at +0.55 V) was the highest with the CuHC10-IB nanoparticles and the lowest with the CuHC10-RT nanoparticles. This is in agreement with the ORR activity observed above.

It should be noted that whereas the electrocatalytic performance of these organically capped copper nanoparticles is subpar as compared to those typically observed with Pt-based nanoparticle catalysts where the onset potentials are generally found to be more positive than +0.90 V and $n \approx 4.0$ [9–11], the activity does show marked enhancement as compared with those of oxygen reduction catalyzed by bulk copper electrodes [22−25]. For instance, in the previous studies with a polycrystalline Cu or CuNi electrode [22,23], the onset potentials for oxygen reduction were found to be around +0.36 V (vs RHE) in a borax buffer solution; and even more negative onset potentials were observed with single-crystalline Cu(100) and Cu(111) electrodes in H_2SO_4 at about 0 V (vs RHE) [24,25]. These are far more negative than those observed above with the decyne-capped copper nanoparticles.

4. Conclusion

Stable alkyne-capped copper nanoparticles were prepared by a simple chemical reduction procedure. TEM measurements showed that the nanoparticles were of 4−6 nm in diameter when the nanoparticles were synthesized at ambient temperature or at 0 °C. The alkyne ligands were found to form Cu−C≡ interfacial bonds at the metal-ligand interface, as manifested in FTIR and photoluminescence measurements. XPS measurements suggested the formation of a small amount of CuO in the nanoparticles, along with Cu_2O. Electrochemical studies indicated that the nanoparticles exhibited apparent electrocatalytic activity in oxygen reduction in alkaline media, with the best performance observed with the samples prepared at 0 °C, in terms of onset potential, the number of electron transfer involved, as well as kinetic current density. Whereas the overall performance remained subpar as compared to that of platinum-based nanoparticle catalysts, the results showed

that nanosized copper was much more active than poly- or single-crystalline bulk copper in the electrocatalytic reduction of oxygen. Notably, the electrocatalytic activity might be further improved by deliberate interfacial engineering of the copper nanoparticles by other metals or chemical ligands. This is the focus of ongoing work and the results will be reported in due course.

Acknowledgments

Appendix A. Supplementary data

Supplementary data related to this article can be found at http://dx.doi.org/10.1016/j.jpowsour.2014.06.054.

References

[1] J. Zhang, PEM Fuel Cell Electrocatalysts and Catalyst Layers : Fundamentals and Applications, Springer, London, 2008.
[2] M. Koper, Fuel Cell Catalysis : a Surface Science Approach, Wiley, Hoboken, N.J, 2009.
[3] I.E.L. Stephens, A.S. Bondarenko, U. Grønbjerg, J. Rossmeisl, I. Chorkendorff, Energy Environ. Sci. 5 (2012) 6744.
[4] H.D. Abruña, F. Matsumoto, J.L. Cohen, J. Jin, C. Roychowdhury, M. Prochaska, R.B. van Dover, F.J. DiSalvo, Y. Kiya, J.C. Henderson, G.R. Hutchison, Bull. Chem. Soc. Jpn. 80 (2007) 1843−1855.
[5] F.T. Wagner, B. Lakshmanan, M.F. Mathias, J. Phys. Chem. Lett. 1 (2010) 2204−2219.
[6] R. Rizo, E. Herrero, J.M. Feliu, Phys. Chem. Chem. Phys. 15 (2013) 15416−15425.
[7] H.H. Wang, Z.Y. Zhou, Q.A. Yuan, N. Tian, S.G. Sun, Chem. Commun. 47 (2011) 3407−3409.
[8] J. Zhang, K. Sasaki, E. Sutter, R.R. Adzic, Science 315 (2007) 220−222.
[9] Z.Y. Zhou, X.W. Kang, Y. Song, S.W. Chen, Chem. Commun. 48 (2012) 3391−3393.
[10] Z.-Y. Zhou, X. Kang, Y. Song, S. Chen, J. Phys. Chem. C 116 (2012) 10592−10598.
[11] K. Liu, X.W. Kang, Z.Y. Zhou, Y. Song, L.J. Lee, D. Tian, S.W. Chen, J. Electroanal. Chem. 688 (2013) 143−150.
[12] J. Suntivich, H.A. Gasteiger, N. Yabuuchi, H. Nakanishi, J.B. Goodenough, Y. Shao-Horn, Nat. Chem. 3 (2011), 647−647.
[13] Y.J. Feng, N. Alonso-Vante, Electrochim. Acta 72 (2012) 129−133.
[14] R. Jasinski, Nature 201 (1964) 1212−1213.
[15] H.G. Jahnke, M. Schonbor, G. Zimmerma, J. Electrochem. Soc. 121 (1974). C120−C120.
[16] K.P. Gong, F. Du, Z.H. Xia, M. Durstock, L.M. Dai, Science 323 (2009) 760−764.
[17] S. Koh, P. Strasser, J. Am. Chem. Soc. 129 (2007) 12624−12625.
[18] P. Mani, R. Srivastava, P. Strasser, J. Phys. Chem. C 112 (2008) 2770−2778.
[19] N.N. Kariuki, X.P. Wang, J.R. Mawdsley, M.S. Ferrandon, S.G. Niyogi, J.T. Vaughey, D.J. Myers, Chem. Mater. 22 (2010) 4144−4152.
[20] H.H. Li, C.H. Cui, S. Zhao, H.B. Yao, M.R. Gao, F.J. Fan, S.H. Yu, Adv. Energy Mater. 2 (2012) 1182−1187.
[21] C.C. Bakir, N. Sahin, R. Polat, Z. Dursun, J. Electroanal. Chem. 662 (2011) 275−280.
[22] M.V. Vazquez, S.R. Desanchez, E.J. Calvo, D.J. Schiffrin, J. Electroanal. Chem. 374 (1994) 189−197.
[23] S. Cere, M. Vazquez, S.R. de Sanchez, D.J. Schiffrin, J. Electroanal. Chem. 505 (2001) 118−124.
[24] G. Brisard, N. Bertrand, P.N. Ross, N.M. Markovic, J. Electroanal. Chem. 480 (2000) 219−224.
[25] T. Jiang, G.M. Brisard, Electrochim. Acta 52 (2007) 4487−4496.
[26] X.-Y. Yan, X.-L. Tong, Y.-F. Zhang, X.-D. Han, Y.-Y. Wang, G.-Q. Jin, Y. Qin, X.-Y. Guo, Chem. Commun. 48 (2012) 1892.
[27] S.W. Chen, A.C. Templeton, R.W. Murray, Langmuir 16 (2000) 3543−3548.
[28] M.J. Hostetler, J.E. Wingate, C.J. Zhong, J.E. Harris, R.W. Vachet, M.R. Clark, J.D. Londono, S.J. Green, J.J. Stokes, G.D. Wignall, G.L. Glish, M.D. Porter, N.D. Evans, R.W. Murray, Langmuir 14 (1998) 17−30.
[29] X.W. Kang, S.W. Chen, Nanoscale 4 (2012) 4183−4189.
[30] Y. Guo, L.M. Chen, Y. Song, P.G. Hu, S.W. Chen, Sci. Adv. Mater. 6 (2014) 1060−1067.
[31] V.I. Mikheeva, N.N. Mal'tseva, J. Struct. Chem. 4 (1963) 643−646.
[32] X.W. Kang, N.B. Zuckerman, J.P. Konopelski, S.W. Chen, J. Am. Chem. Soc. 134 (2012) 1412−1415.
[33] D.R. Lide, CRC Handbook of Chemistry and Physics : a Ready-reference Book of Chemical and Physical Data, 85th ed., CRC Press, Boca Raton, Fla, 2004.
[34] T. Ghodselahi, M.A. Vesaghi, A. Shafiekhani, A. Baghizadeh, M. Lameii, Appl. Surf. Sci. 255 (2008) 2730−2734.
[35] C.D. Wagner, W.M. Riggs, L.E. Davis, J.F. Moulder, G.E. Muilenberg, Handbook of X-ray Photoelectron Spectroscopy: a Reference Book of Standard Data for Use in X-ray Photoelectron Spectroscopy, Perkin-Elmer Corp, Eden Prairie, Minn., 1979.
[36] K.S. Kim, J. Elecctron Spec. Rel. Phen. 3 (1974) 217−226.
[37] S.M.A. Elhaleem, B.G. Ateya, J. Electroanal. Chem. 117 (1981) 309−319.
[38] A.J. Bard, L.R. Faulkner, Electrochemical Methods: Fundamentals and Applications, second ed., John Wiley, New York, 2001.